Journal of Turbulence

ISSN: (Print) 1468-5248 (Online) Journal homepage: http://www.tandfonline.com/loi/tjot20

Acceleration statistics of prolate spheroidal particles in turbulent channel flow

Rafik Ouchene, Juan Ignacio Polanco, Ivana Vinkovic & Serge Simoëns

To cite this article: Rafik Ouchene, Juan Ignacio Polanco, Ivana Vinkovic & Serge Simoëns (2018) Acceleration statistics of prolate spheroidal particles in turbulent channel flow, Journal of Turbulence, 19:10, 827-848, DOI: 10.1080/14685248.2018.1516043

To link to this article: https://doi.org/10.1080/14685248.2018.1516043

Published online: 09 Sep 2018.

JOURNAL OF TURBULENCE
2018, VOL. 19, NO. 10, 827–848
https://doi.org/10.1080/14685248.2018.1516043

Taylor & Francis
Taylor & Francis Group

Check for updates

Acceleration statistics of prolate spheroidal particles in turbulent channel flow

Rafik Ouchene, Juan Ignacio Polanco, Ivana Vinkovic and Serge Simoëns

Laboratoire de Mécanique des Fluides et d'Acoustique, Université de Lyon, Villeurbanne Cedex, France

ABSTRACT

Computation of a dilute suspension of prolate spheroidal particles in a turbulent channel flow is undertaken to study the influence of inertia and shape on acceleration statistics. A pseudo-spectral direct numerical simulation is coupled with Lagrangian tracking under the one-way coupling assumption. Simulations are carried out at friction Reynolds number $Re_\tau = 1440$, for three aspect ratios $\lambda = 1, 3$ and 10, and two Stokes numbers $St = 5$ and 30. Results indicate that, as a consequence of the filtering effect of inertia, particle acceleration RMS decreases with increasing inertia. In addition, the normalised streamwise acceleration PDFs depart from that of the conditional fluid and their tails become narrower as inertia is increased. Furthermore, acceleration statistics show that particle elongation has a significant effect on the mean drag and on the particle selective sampling. Moreover, the classification of elongated particle behaviour in turbulent channel flow based on a global Stokes number is questioned. The zero-crossing acceleration autocorrelation timescales presented points out the need for a local dimensionless number estimation adapted to the case of prolate spheroids.

ARTICLE HISTORY
Received 28 May 2018
Accepted 18 August 2018

KEYWORDS
DNS; spheroidal particles; acceleration statistics

1. Introduction

Widely present in many environmental and industrial applications such as pollen transport [1], micro-organism turbulent dispersion [2] or wood fibres in paper pulp [3], non-spherical particle transport in turbulent flows has been increasingly investigated in numerous experimental and numerical studies. Since particles can have an indefinite possibility of shapes and sizes, focus has been put on spheroidal particles that can describe both elongated (fibres of cellulose pulp or straw) and flattened particles (flakes or wood chips).

Non-spherical particle motion has been widely investigated in the last decades. An interesting analysis of the different investigations has been provided by Voth and Soldati [4]. The authors reviewed the models used to describe non-spherical particle motion, along with numerical and experimental methods for measuring particle dynamics. Restricting the discussion to the transport of spheroids in wall-bounded turbulent flow, Zhang et al. [5]

CONTACT Rafik Ouchene r.ouchene1@gmail.com Laboratoire de Mécanique des Fluides et d'Acoustique, Université de Lyon, Université Claude Bernard Lyon 1, Ecole Centrale de Lyon, INSA de Lyon, CNRS UMR 5509, 43Boulevard du 11 novembre 1918, Villeurbanne Cedex 69622, France

investigated the motion of inertial ellipsoids in an inhomogeneous turbulent flow provided by direct numerical simulations (DNS). The authors showed that particle shape can greatly modulate deposition on the walls. Considering a dilute suspension of particles, Mortensen et al. [6,7], Marchioli et al. [8] and Zhao et al. [9,10] tracked prolate ellipsoids with varying inertia and aspect ratios in turbulent channel flow DNS. They found that, similar to spherical particles, ellipsoids tend to accumulate in the viscous sublayer and preferentially sample regions of low-speed fluid velocity. In addition, ellipsoidal particles exhibit preferential alignment with the mean flow, particularly near the wall. Interestingly, in all these studies, it has been shown that statistics of the translational velocity are not significantly affected by particle shape, whereas rotational motion displays a substantial dependence on the aspect ratio. To examine the role of particle shape on particle-turbulence interaction, focusing on the slip velocity between the particles and the viscous carrier fluid, Zhao et al. [11] performed DNS under the one-way coupling assumption, for a large range of particle inertia and aspect ratios. They showed that slip velocity statistics can be quantitatively affected by particle elongation for small particle inertia. This effect vanishes as inertia increases. For all of these numerical investigations, the hydrodynamic force and torque are predicted using the analytical expressions derived by Jeffery [12] and Happel and Brenner [13]. These analytical expressions are strictly valid when the particle Reynolds number tends to zero. Including the empirical formulas for the non-linear hydrodynamic force and torque, Ouchene et al. [14] performed DNS for prolate ellipsoids. The authors showed that including non-linear hydrodynamic forces, when the particle Reynolds number is of the order of unity, does not lead to any significant deviation of the velocity statistics from values predicted by the linear drag force. However, in a vertical wall-bounded turbulent flow [15], where gravity is opposite to the mean flow direction, Ouchene et al. [15] found a significant alteration of translational and rotational velocity statistics.

While translational and rotational velocity statistics have been widely investigated in literature, as described above, acceleration statistics of non-spherical particles in turbulent channel flows remain unexplored. In the case of spherical particles, the main relevant effects that have been revealed in previous studies consist on particle clustering, i.e. the tendency of particles to sample strain-dominated regions [16], and on the inertia filtering effect. Namely, inertia acts as a low-pass filter of the surrounding fluid velocity variations [17]. From DNS coupled with Lagrangian pointwise particle tracking, Bec et al. [17] noticed that, even for small inertia, spherical particles are expelled from regions with strong acceleration fluctuations in the case of homogeneous isotropic turbulence (HIT). In addition, Bec et al. [17] showed that the probability density functions (PDFs) of spherical particle acceleration are highly non-Gaussian. These PDFs tend to Gaussianity when inertia is increased. Furthermore, increasing inertia leads to a monotonic decrease of the particle acceleration variance. Ayyalasomayajula et al. [18] confirmed these observations through measurements of water droplet acceleration in wind-tunnel turbulence. The authors found heavier tails of the PDFs and decreasing of particle acceleration variance when inertia is increased. They also suggested that the coupling between clustering and filtering has a substantial effect on spherical particle acceleration statistics.

Experimentally, in the case of a turbulent wall-bounded flow, Gerashchenko et al. [19] noticed that the spherical particle mean deceleration and its root mean square (RMS) increase to large values close to the wall. These effects are more pronounced as the Stokes number is increased. In the wall-normal direction, only slight downward mean deceleration and its RMS have been observed by Gerashchenko et al. [19]. This was attributed to the non-trivial interaction of the inertial particles with boundary layer structures and gravity. To investigate this issue, Lavezzo et al. [20] performed direct numerical simulations of a dilute spherical suspension in turbulent channel flow. Their DNS results were in good agreement with the results given by Gerashchenko et al. [19], confirming the experimental observations. In addition, Lavezzo et al. [20] isolated and quantified the effect of gravitational settling. The authors showed that the crossing trajectories effect influences acceleration statistics of pointwise inertial spherical particles in a horizontal boundary layer. In turbulent channel flow, Zamansky et al. [21] examined the acceleration statistics of spherical pointwise particles, as well as fluid acceleration statistics unconditioned and conditioned to the presence of particles. The authors claimed that, while the wall-normal and spanwise components of the RMS of the conditional fluid acceleration remain close to the unconditional fluid acceleration, the conditional streamwise RMS is remarkably higher in the near-wall region. The authors also found that, in accordance with earlier studies, when inertia is increased, PDFs of particle acceleration scaled by the acceleration RMS depart from that of the fluid and the tails of these PDFs become narrower.

Particle acceleration is directly related to the net force the particle experiences along its trajectory. This aerodynamic force depends on particle shape and orientation when the particles are non-spherical. Therefore, shape effects on acceleration statistics are investigated here to understand the dynamics of non-spherical particles in turbulent flows. To our knowledge, only Njobuwenwu and Fairweather [22] reported the PDFs of the normalised wall-normal spheroidal particle acceleration at two wall distances, in the channel centre and the buffer region. The authors used large-eddy simulations at a friction Reynolds number of $Re_\tau = 300$ coupled with Lagrangian tracking of needle- and platelet-like particles in a turbulent channel flow. In the case of oblate and prolate particles with respective aspect ratios $\lambda = 10^{-1}$ and 10 and an equivalent Stokes number of $St = 125$, the authors found that the tails of the wall-normal acceleration PDFs are not significantly affected by shape compared to the spherical case, although differences may occur at the peak value.

In view of this discussion, the aim of this study is to examine the combined effect of wall turbulence, particle inertia and shape on prolate spheroidal particle acceleration statistics. This issue is investigated through a direct numerical simulation coupled with Lagrangian particle tracking (DNS/LPT) under the one-way coupling assumption in the absence of gravity. Prolate spheroidal particles with varying inertia and aspect ratios are studied. Fluid acceleration statistics conditioned on the presence of particles are analysed, in order to describe fluid regions where particles accumulate.

The paper is organised as follows. Section 2 is devoted to the numerical method and physical parameters. Section 3 deals with average acceleration statistics. In Section 4, the acceleration RMS is discussed. Acceleration PDFs and autocorrelations are presented in Sections 5 and 6, respectively. Section 7 is devoted to the conclusion.

2. Numerical method

2.1. Flow

In the present study, we consider an incompressible, isothermal, Newtonian fluid moving between two fixed, parallel walls with distance $2h$. The flow is governed by the continuity

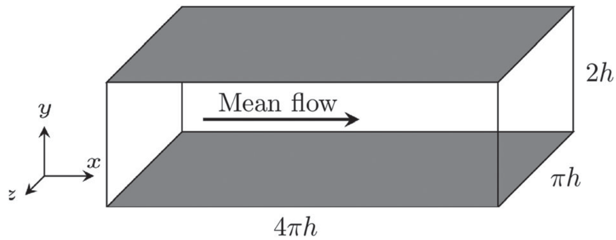

Figure 1. Computational domain Γ.

and the Navier–Stokes equations. After scaling by the velocity at the channel centre U_0, and by the channel half-height h, and by the fluid density ρ the governing equations read:

$$\nabla \cdot \mathbf{u} = 0 \quad \text{for } \mathbf{x} \in \Gamma \tag{1}$$

$$\frac{\partial \mathbf{u}}{\partial t} + \mathbf{u} \cdot \nabla \mathbf{u} = -\nabla p + \frac{1}{Re} \Delta \mathbf{u} \quad \text{for } \mathbf{x} \in \Gamma \tag{2}$$

where $\mathbf{u}(x, y, z, t)$ is the velocity vector, $p(x, y, z, t)$ the pressure and $Re = U_0 h/\nu$ the Reynolds number based on thecentreline velocity, with ν the kinematic viscosity of the fluid. The computational domain Ω is defined by $[0, L_x] \times [0, 2h] \times [0, L_z]$ respectively in the streamwise, wall-normal and spanwise directions (Figure 1). The no-slip velocity condition is used on the walls while periodic boundary conditions are applied in the streamwise x and spanwise z directions. Equations (1) and (2) are solved using a Galerkin spectral approximation (Fourier–Chebyshev) and a variational projection method on a divergence-free space as described in [23].

2.2. Particles

To consider dilute systems, prolate spheroidal particles are injected into the flow at low volume fractions. Spheroids are characterised by the aspect ratio, λ, which is defined as the ratio between the revolution axis diameter and the small axis diameter $2a$. The translational motion of spheroidal particles is given by the Newton equations:

$$\rho_p V_p \frac{\mathrm{d}\mathbf{u_p}}{\mathrm{d}t} = \mathbf{F} \tag{3}$$

where $\mathbf{u_p}$ is the particle velocity vector, ρ_p is the spheroid density, V_p is the volume of the spheroid and $\mathbf{F}$ is the hydrodynamic force acting on the spheroid. For small heavy particles ($\rho_p >> \rho$), the Maxey and Riley [24] formulation for the forces acting on the particles reduces to the drag force, $\mathbf{F_D}$ [25]. Under creeping flow conditions, the expression of the hydrodynamic drag is given by Happel and Brenner [13] as

$$\mathbf{F_D} = \mu \mathbf{A}^{\mathbf{t}} \mathbf{K}'' \mathbf{A}(\mathbf{u}(\mathbf{x_p}, t) - \mathbf{u}_p) \tag{4}$$

where μ is the fluid dynamic viscosity, $\mathbf{u}(\mathbf{x_p}, t)$ is the fluid velocity at the particle position $\mathbf{x_p}$ and $\mathbf{K}''$ is the resistance tensor in the particle frame $\mathbf{x} = \langle x'', y'', z'' \rangle$ (Figure 2),

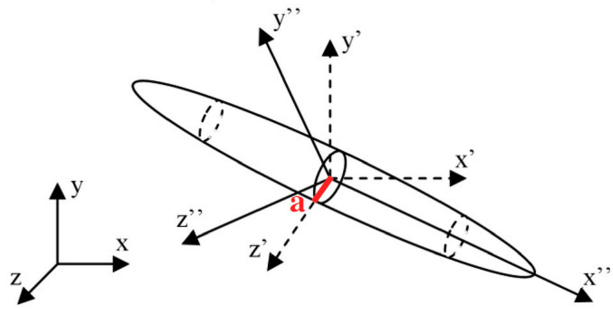

Figure 2. Cartesian coordinate systems for the spheroidal particles.

given by

$$\mathbf{K}'' = \begin{pmatrix} K''_{x''x''} & 0 & 0 \\ 0 & K''_{y''y''} & 0 \\ 0 & 0 & K''_{z''z''} \end{pmatrix} \tag{5}$$

where

$$\begin{aligned} K''_{x''x''} &= \frac{8(\lambda^2 - 1)^{3/2}}{(2\lambda^2 - 1)\ln(\lambda + \sqrt{\lambda^2 - 1}) - \lambda\sqrt{\lambda^2 - 1}} \\ K''_{y''y''} = K''_{z''z''} &= \frac{16(\lambda^2 - 1)^{3/2}}{(2\lambda^2 - 3)\ln(\lambda + \sqrt{\lambda^2 - 1}) + \lambda\sqrt{\lambda^2 - 1}} \end{aligned} \tag{6}$$

In Equation (4), $\mathbf{A}$ is the orthogonal transformation matrix:

$$\mathbf{A} = \begin{pmatrix} 1 - 2(e_2^2 + e_3^2) & 2e_1e_2 - 2e_0e_3 & 2e_0e_2 + 2e_1e_3 \\ 2e_1e_2 + 2e_0e_3 & 1 - 2(e_1^2 + e_3^2) & 2e_2e_3 - 2e_0e_1 \\ 2e_1e_3 - 2e_0e_2 & 2e_0e_1 + 2e_2e_3 & 1 - 2(e_1^2 + e_2^2) \end{pmatrix} \tag{7}$$

and $\mathbf{A}^{\mathrm{t}}$ is its transpose defined by the Euler parameters of the quaternion $\mathbf{q}(e_0, e_1, e_2, e_3)$. These parameters must satisfy $e_0^2 + e_1^2 + e_2^2 + e_3^2 = 1$.

The rotational motion of a spheroid is given by

$$\frac{\mathrm{d}\mathbf{I} \cdot \mathbf{\Omega}''}{\mathrm{d}t} + \mathbf{\Omega}'' \times (\mathbf{I} \cdot \mathbf{\Omega}'') = \mathbf{T}'', \tag{8}$$

where $\mathbf{I}$ is the inertia tensor, $\mathbf{\Omega}''$ is the angular velocity of the spheroid, and $\mathbf{T}''$ the rotational torque acting on the ellipsoid. Thus, the translational and rotational motion of spheroidal particles in dimensionless form read as [5,8]

$$\text{Kinematics}\begin{cases} \dfrac{\mathrm{d}\mathbf{x_p}}{\mathrm{d}t} = \mathbf{u}_p \\ \dfrac{\mathrm{d}e_0}{\mathrm{d}t} = \dfrac{1}{2}(-e_1\Omega_{x''} - e_2\Omega_{y''} - e_3\Omega_{z''}) \\ \dfrac{\mathrm{d}e_1}{\mathrm{d}t} = \dfrac{1}{2}(e_0\Omega_{x''} - e_3\Omega_{y''} + e_2\Omega_{z''}) \\ \dfrac{\mathrm{d}e_2}{\mathrm{d}t} = \dfrac{1}{2}(e_3\Omega_{x''} + e_0\Omega_{y''} - e_1\Omega_{z''}) \\ \dfrac{\mathrm{d}e_3}{\mathrm{d}t} = \dfrac{1}{2}(-e_2\Omega_{x''} + e_1\Omega_{y''} + e_0\Omega_{z''}) \end{cases} \tag{9}$$

$$\text{Dynamics}\begin{cases} \rho_p V_p \dfrac{\mathrm{d}\mathbf{u_p}}{\mathrm{d}t} = \mathbf{F} \\ \dfrac{\mathrm{d}\Omega_{x''}}{\mathrm{d}t} = \dfrac{20(\omega_{x''x''} - \Omega_{x''})}{2\beta_0^2 \frac{\rho_p}{\rho} a^2} \\ \dfrac{\mathrm{d}\Omega_{y''}}{\mathrm{d}t} = \Omega_{x''}\Omega_{z''}\left(1 - \dfrac{2}{1+\lambda^2}\right) + \dfrac{20((1-\lambda^2)D_{x''z''} + (1+\lambda^2)(\omega_{y''y''} - \Omega_{y''}))}{(\gamma_0 + \lambda^2\alpha_0)(1+\lambda^2)\frac{\rho_p}{\rho} a^2} \\ \dfrac{\mathrm{d}\Omega_{z''}}{\mathrm{d}t} = \Omega_{x''}\Omega_{y''}\left(1 - \dfrac{2}{1+\lambda^2}\right) + \dfrac{20((1-\lambda^2)D_{y''z''} + (1+\lambda^2)(\omega_{z''z''} - \Omega_{z''}))}{(\beta_0 + \lambda^2\alpha_0)(1+\lambda^2)\frac{\rho_p}{\rho} a^2} \end{cases} \tag{10}$$

Here, D_{ij} and ω_{ij} are respectively the elements of the fluid rate of strain and rotation tensor in the particle frame :

$$\begin{aligned} \omega_{ij} &= \frac{1}{2}\left(\frac{\partial u_i''}{\partial x_j''} - \frac{\partial u_j''}{\partial x_i''}\right) \\ D_{ij} &= \frac{1}{2}\left(\frac{\partial u_i''}{\partial x_j''} + \frac{\partial u_j''}{\partial x_i''}\right) \end{aligned} \tag{11}$$

The parameters α_0, β_0 and γ_0 are given by Gallily and Cohen [26] as

$$\begin{aligned} \alpha_0 &= -\frac{2}{\lambda^2 - 1} - \frac{\lambda}{(\lambda^2-1)^{3/2}} \ln\left(\frac{\lambda - \sqrt{(\lambda^2-1)}}{\lambda + \sqrt{(\lambda^2-1)}}\right) \\ \beta_0 = \gamma_0 &= \frac{2}{\lambda^2 - 1} + \frac{\lambda}{2(\lambda^2-1)^{3/2}} \ln\left(\frac{\lambda - \sqrt{(\lambda^2-1)}}{\lambda + \sqrt{(\lambda^2-1)}}\right) \end{aligned} \tag{12}$$

The Stokes number characterises the response time of a solid particle to solicitations by a turbulent flow. In the case of a spherical particles $\lambda = 1$, the Stokes number is given by

$$St = \frac{\tau_p}{\tau_f} \tag{13}$$

where $\tau_p = \rho_p d_p^2/18\rho\nu$ is the characteristic relaxation time of solid spherical particles used in pointwise particle models [21], and $\tau_f = \nu/u_\tau^2$ is a characteristic fluid time scale. Therefore, $St = \tau_p/\tau_f$ can be interpreted as a characteristic particle timescale in wall units, τ_p^+. In

Table 1. Flow simulation parameters.

Re_τ	Re	$N_x \times N_y \times N_z$	$L_x \times L_y \times L_z$	$\Delta x^+ \times \Delta y^+ \times \Delta z^+$	Δt^+
1440	34,000	2048 × 432 × 1024	$4\pi h \times 2h \times \pi h$	8.8 × (0.03 ∼ 10.5) × 2.2	0.033

Table 2. Particle parameters.

Case	ρ_p/ρ	λ	St	N_p	a^+	$\phi(10^{-7})$
$C1$	769.23	1.001	5	200,000	0.171	0.2
$C2$	769.23	3	5	200,000	0.125	0.2
$C3$	769.23	10	5	200,000	0.098	0.3
$C4$	769.23	1.001	30	200,000	0.419	2.6
$C5$	769.23	3	30	200,000	0.306	3.1
$C6$	769.23	10	30	200,000	0.241	5.0

the case of prolate spheroidal particles $\lambda > 1$, the characteristic time in wall units is given according to Shapiro and Goldenberg [27] by

$$\tau_p^+ = St = \frac{4\lambda\rho_p {a^+}^2}{18\rho} \frac{\ln(\lambda + \sqrt{\lambda^2 - 1})}{\sqrt{\lambda^2 - 1}} \tag{14}$$

where a^+ is the dimensionless semi-minor axis.

2.3. Simulation parameters

The simulations are performed for Reynolds number $Re = 34,000$. This corresponds to a Reynolds number based on the friction velocity u_τ, $Re_\tau = u_\tau h/\nu = 1440$. Parameters of simulations are reported in Table 1, where N_i and L_i are respectively the number of grid points and the domain length in direction i. The superscript '+' denotes quantities expressed in wall units normalised by the friction velocity u_τ and viscosity ν.

Simulations are carried out for six different particle sets. In all cases, 200,000 particles are injected randomly into the flow. To fix the value of the response time, St, for the different aspect ratios, the density ratio ρ_p/ρ is kept constant. The Stokes numbers and aspect ratios are respectively $St = 5$ and 30 and $\lambda = 1$, 3 and 10. Values for the different particle parameters studied here are given in Table 2.

To solve the translational and rotational motion a mixed differencing procedure is used [28]. A second order Adams-Bashforth scheme is applied to solve Equation (9). For each particle, Euler parameters are renormalised after every time step. Particle equations are solved using the same time step as for the Navier–Stokes equations. The fluid velocity, acceleration and its gradients are computed at the particle location using a third-order Hermite interpolation [29]. Initially, each particle has the velocity and angular velocity of the fluid at the same position. Periodic boundary conditions are applied in the homogeneous directions, while elastic rebounds are used when the distance between the mass centre of the ellipsoid and the wall is less or equal to the semi-minor axis. In this study, particle orientation is not accounted for in the wall-collision model. Except in some studies [30] , this approximation is widely used for particle/wall interactions. Even if the model is quite unrealistic, it is expected that the number of wall collisions is not high enough to significantly alter the particle translational and rotational statistics [5,6,15]. Gravity is not considered in the present work.

The aim here is to analyse the influence of inertia and shape on acceleration statistics and compare the results to previous findings on spherical particles in the absence of gravity. In future work, this can be very useful for isolating and quantifying the effect of gravitational settling alone.

Particle statistics are obtained as follows. The domain is divided into wall-parallel slabswith thickness equal to the wall-normal grid spacing. Results for each variable areaveraged over all particles belonging to the same wall-parallel slab. In addition, resultsare averaged in time over $t^+ \in [1500-1800]$. The different statistics of the spanwise component of theacceleration show a zero value or the same behaviour as the wall-normalcomponent. Hence, for the sake of brevity, only the streamwise and wall-normalstatistics are discussed here.

3. Particle concentration

To gain insight into inertial spheroids segregation in a wall-bounded turbulent flow, thenormalised particle number density $\langle Cp \rangle$ is reported in Figure 3 against the wall distance. This parameter is defined as the time-average ratio between the number of particles in each slab per unit volume, $N_{p,\mathrm{Slab}}/V_{\mathrm{Slab}}$, and the total number of particles per volume, N_p/V_{Channel}:

$$\langle Cp \rangle = \frac{N_{p,\mathrm{Slab}}/V_{\mathrm{Slab}}}{N_p/V_{\mathrm{Channel}}} \tag{15}$$

Here, we used 192 slabs parallel to xz plane and distributed according to a cosine law, given by the Chebyshev grid distribution.

Despite the initial uniform distribution of particles, Figure 3 shows clearly the tendency of inertial spheroids to accumulate in the near-wall region. This accumulation is more pronounced as inertia is increased. The tendency of inertial particles to accumulate in the near-wall region where the turbulence intensity is smaller is known for spherical particles as 'turbophoresis' [31]. In addition, a shape effect is clearly noticeable for $St = 5$ while it is mitigated for $St = 30$. This means that, as for spherical particles at higher inertia, spheroids segregation is mainly a consequence of the combined effects of inertia and wall turbulence. The average particle concentration depends on the slab thickness and distribution. In addition, close to the wall, particle number density depend also on particle size. Indeed, due

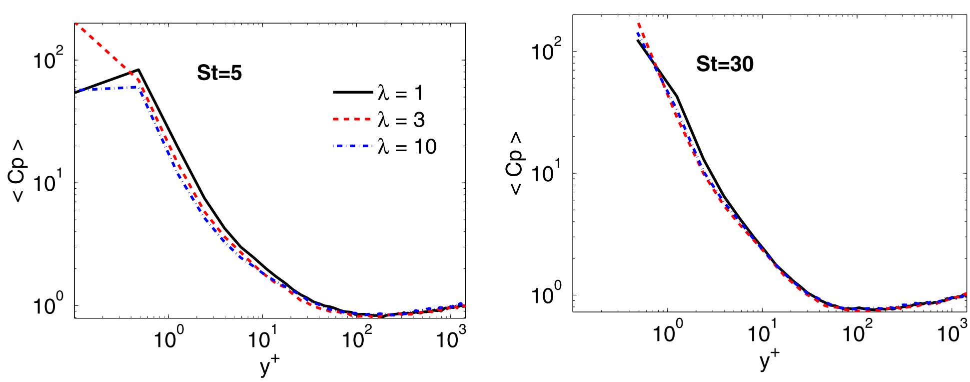

Figure 3. Normalised mean particle number density as a function of wall distance.

to the slab thickness and to the different semi-minor radii (Table 2), plots start at different wall distances for $St = 5$ ($a^+ = 0.096$) and for $St = 30$ ($a^+ = 0.48$).

As mentioned above, for $St = 5$ there is a noticeable shape effect on particle concentration. Close to the wall, for $y^+ < 1$, spherical particles ($\lambda = 1$) present the highest concentration, whereas particles with $\lambda = 10$ have the lowest C_p. On the wall, for $y^+ > 1$, a non-monotonic behaviour of particle concentration with the aspect ratio is observed, with $\lambda = 3$ particles presenting the highest concentration. This is an interesting feature resulting probably from the interplay of aspect ratio (rotation and translation statistics) and particle segregation on the wall. It is not due to the wall-collision model, since when particles collide with the wall, particle orientation is not accounted for, as mentioned earlier. This non-monotonic evolution of the particle concentration has also been found in a previous study by Marchioli et al. [8]. Here, only translational and rotational particle velocity statistics have reached a steady state. Particle concentration profiles have not yet reached the steady state and the number of particles on the wall still depends on time. The particle concentration profiles given in Figure 3 are only used here to show the beginning of particle segregation towards the wall.

4. Mean acceleration

The mean streamwise and wall-normal accelerations of the particles and fluid seen by the particles are reported in Figures 4 and 5. As fluid seen by the particles, we refer to fluid statistics conditioned on the presence of prolate spheroids. For comparison, the mean acceleration of the unconditioned fluid is also plotted.

Figure 4 shows that the streamwise acceleration of the particles is negative in thenear-wall region ($y^+ < 25$) and positive in the core of the channel. This indicates that, moving to the wall, particles present a higher streamwise velocity than the surrounding fluid and therefore are decelerated. Whereas, when particles move away from the wall their mean streamwise velocity is lower than that of the surrounding fluid and are accordingly accelerated. This trend is well known from the mean velocity profile [32] and relative velocity [11] and interpreted as a change of the direction of drag force with respect to distance from the wall. In addition, accelerations of the particles and the fluid seen by the particles depart significantly from the unconditional fluid acceleration. Indeed, particle deceleration decreases with increasing particle inertia. Contrarily, deceleration of the fluid seen by the particles increases with increasing particle inertia. This indicates that, drifting towards the wall, particles with $St = 5$ sample turbulent regions with small deceleration while particles with $St = 30$ preferentially accumulate in regions with higher deceleration. To reach the surrounding fluid velocity, particles with $St = 5$ respond faster than $St = 30$ to the fluid solicitations, and accordingly, present higher deceleration. Moreover, particle deceleration exceeds that of the conditional and unconditional fluid, in the viscous sublayer region. Clearly, the consequence of the particle accumulation and preferential concentration, in the viscous sublayer, is an increase of particle mean deceleration compared to the fluid.

Regarding the effect of particle shape, significant differences between the spheroidal and the spherical particles can be observed, especially, in the near-wall region. Particle deceleration increases for $\lambda = 3$ compared to the spherical particles, while only slight deviation is observed between particles with $\lambda = 3$ and 10. This is also observed for the conditional fluid, implying that spherical and elongated particles do not see, statistically, the same fluid

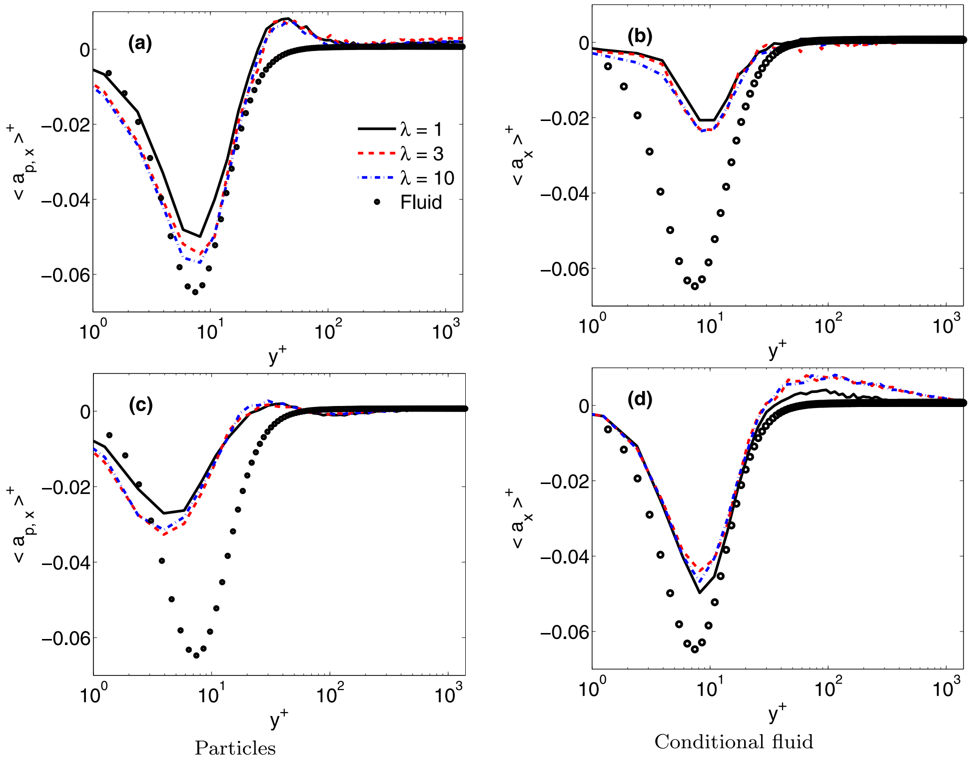

Figure 4. Mean streamwise acceleration for particles (left) and fluid at particle position (right) for different aspect ratios λ. Black dots represent the unconditioned fluid acceleration. Top figures (a,b) show $St = 5$, bottom figures (c,d) show $St = 30$.

acceleration. Interestingly, while the translational and rotational velocity statistics of the conditional fluid were found unaffected by particle elongation [6,14], the conditional fluid acceleration is influenced by particle shape.

In contrast to the streamwise acceleration component, average wall-normal acceleration of the particles, and of the conditional and unconditional fluid exhibit a positive acceleration in the near-wall region and a negative one in the core of the channel (Figure 5). This means that, in the near-wall region, wall-normal drag acts opposite to the direction of particle segregation and counteracts the drifting of particles to the wall. In the core of the channel, particles move away from the wall and experience weak negative mean wall-normal drag. As for the streamwise component, acceleration of the particles and fluid seen shows a significant departure from the unconditioned fluid. In addition, the inertia filtering effect occurs for both Stokes numbers leading to a decrease of the wall-normal particle acceleration with increasing inertia. Our observations on fluid and particle accelerations in both streamwise and wall-normal directions are in good agreement with the results found by Zamansky et al. [21] in the case of spherical pointwise particles. However, the mean acceleration of the conditioned fluid was not provided by the authors. Furthermore, the profile of the particles mean wall-normal acceleration exhibit roughly the same trend whatever the aspect ratio, suggesting that this acceleration component is weakly altered by particle elongation. This is not the case for the conditional fluid wall-normal acceleration,

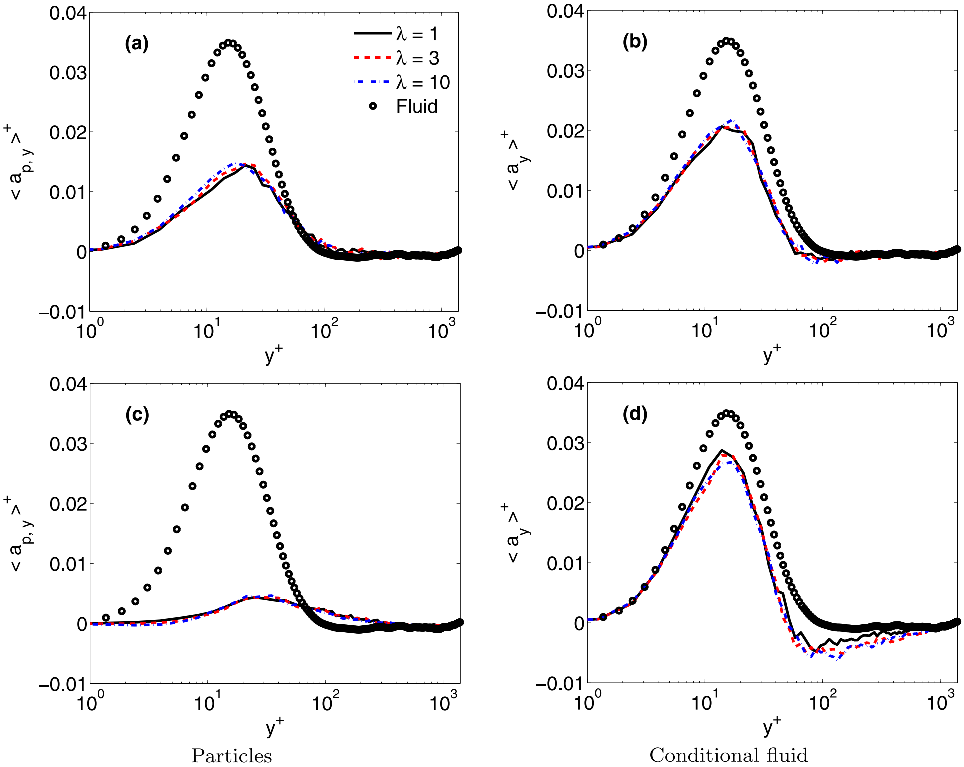

Figure 5. Mean wall-normal acceleration for particles (left) and fluid at particle position (right) for different aspect ratios λ. Black dots represent the unconditioned fluid acceleration. Top figures (a,b) show $St = 5$, bottom figures (c,d) show $St = 30$.

which is influenced by particle shape, especially, for $St = 30$. This influence is more pronounced for $St = 30$, suggesting that, at higher inertia, spheroids with different elongations do not see, statistically, the same wall-normal fluid acceleration.

5. Acceleration RMS

Streamwise and wall-normal acceleration RMS are respectively plotted in Figures 6 and 7. The RMS of the unconditioned fluid acceleration is also provided on all plots (black circles). The streamwise component (Figure 6) shows that particle acceleration RMS can exceed that of the fluid in the near-wall region for $St = 5$, whereas, it is decreased compared to the fluid for the higher inertia case. Sweeps and ejections govern particle transfer in the wall-normal direction and lead to a modulation of the flow field seen by the particles [31,33,34]. Bec et al. [17] noticed in HIT that inertial pointwise spherical, particles are expelled from turbulent regions with high acceleration fluctuations. However, Zamansky et al. [21] found that, in wall-bounded turbulence, inertial particles can concentrate in turbulent regions with high streamwise acceleration fluctuations. According to the authors, the physical mechanism behind this trend is the intermittency of high-and-low speed streaks which leads to strong variations of the streamwise fluid velocity. Although for $St = 30$, particles are also subjected to this intermittency, particles with higher inertia

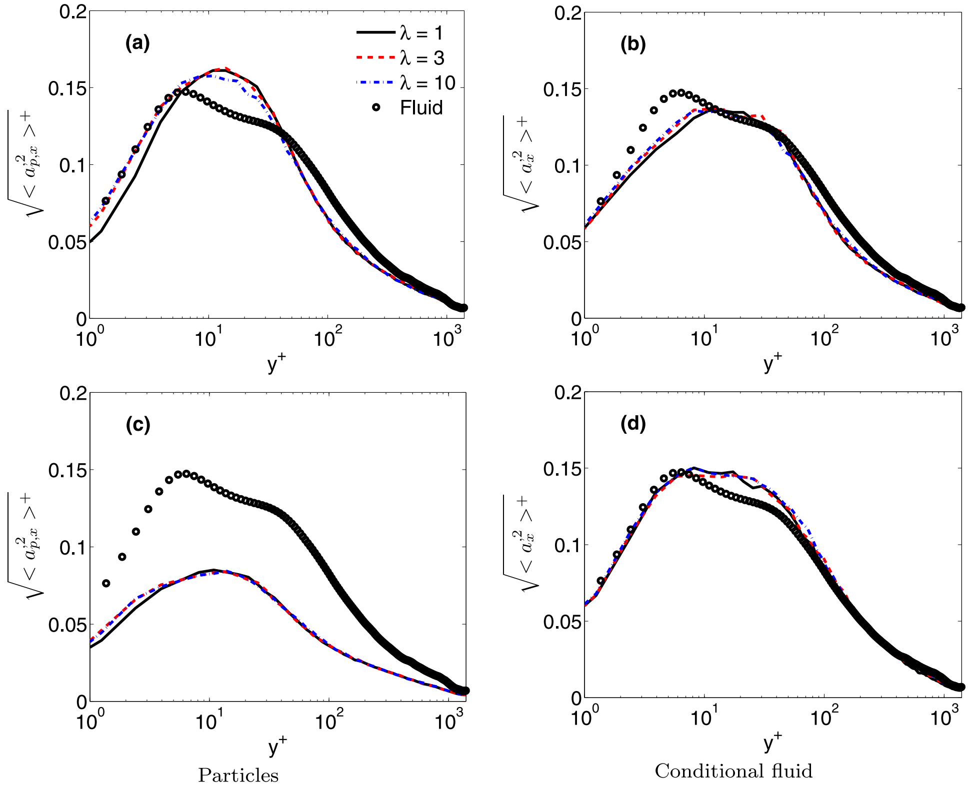

Figure 6. Streamwise acceleration RMS for particles (left) and fluid at particle position (right) for different aspect ratios λ. Black dots represent the unconditioned fluid acceleration. Top figures (a,b) show $St = 5$, bottom figures (c,d) show $St = 30$.

respond slowly to the fluid solicitations, and consequently present lower fluctuations of the streamwise acceleration. Regarding the fluid seen by the particles, particles statistically sample regions of high streamwise acceleration fluctuations. This trend is more pronounced as inertia is increased. These results are, qualitatively, in agreement with observations by Zamansky et al. [21] for pointwise spherical particles. However, from a quantitative point of view, the results given in [21] for the fluid seen are much higher than the unconditional fluid (about 3/2 at the peak). Furthermore, particle shape does not lead to any significant deviation from the spherical case for the conditional fluid, whereas, the RMS of the particle acceleration increases, with increasing aspect ratio, in the viscous sublayer. As previously noticed for velocity statistics [6,14], we find here that the influence of particle shape on prolate acceleration streamwise RMS is mostly present in the viscous sublayer. The wall-normal particle acceleration RMS profiles, depicted in Figure 7, exhibit a pronounced dependence on inertia since a significant decrease of the acceleration RMS is observed when inertia is increased, as for spherical particles [20,21]. This is attributed to the inertia filtering effect that mitigates particle acceleration fluctuations compared to that of the surrounding fluid. As for the streamwise acceleration RMS, the wall-normal acceleration fluctuations of the conditioned fluid increase with increasing particleinertia. However, these fluctuations remain of the same order or less than the unconditioned fluid

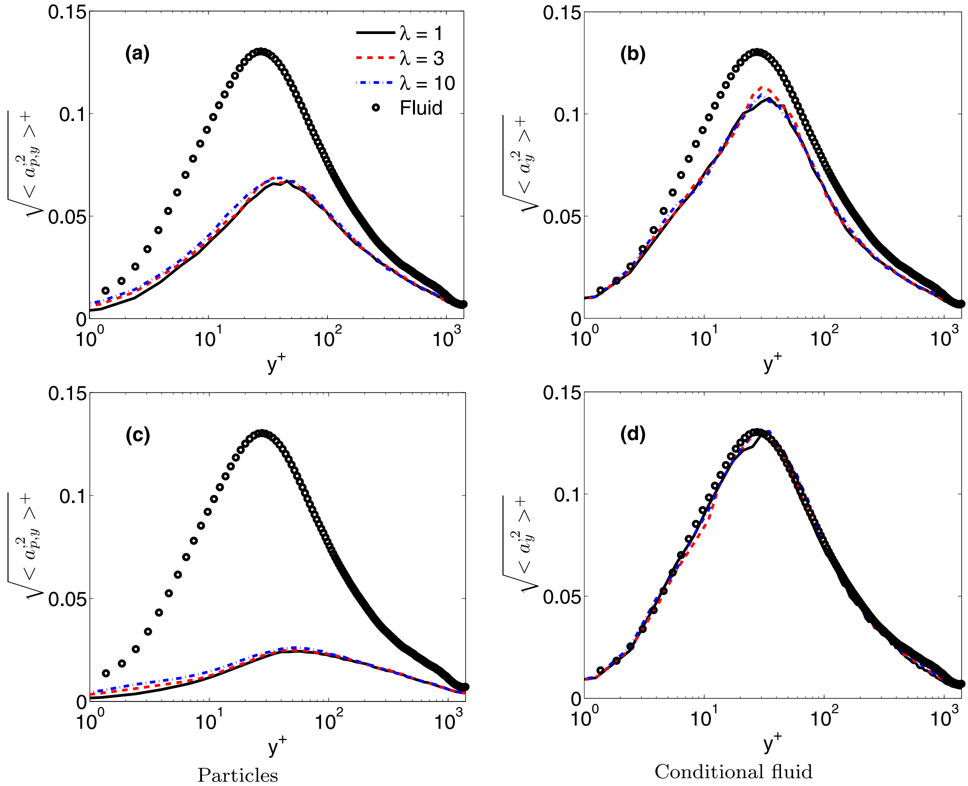

Figure 7. Wall-normal acceleration RMS for particles (left) and fluid at particle position (right) for different aspect ratios λ. Black dots represent the unconditioned fluid acceleration. Top figures (a,b) show $St = 5$, bottom figures (c,d) show $St = 30$.

acceleration RMS. This means that particles with higher inertiaselectively sample regions of high acceleration fluctuations remaining less responsiveto these fluid solicitations. Moreover, the particle wall-normal acceleration RMS increases monotonically with increasing aspect ratio. This shape effect becomes more pronounced for the higher inertia case at $y^+ < 50$. The wall-normalacceleration of the fluid seen by the particles does not exhibit a discernible shape effect implying that particles see statistically the same fluid acceleration fluctuations while they react differently to these solicitations. Interestingly, whateverthe direction, the particle acceleration RMS exceeds the corresponding mean acceleration by roughly 2–5 times revealing that a frequent changeof sign of the drag force can be expected. This observation is also reportedby Zhao et al. [35] for statistics of the relative velocity of spherical particles. An interesting additional feature, for the acceleration statistics analysis, is theacceleration norm. Figure 8 illustrates the profiles of the acceleration norm mean and RMS values. Both Stokes numbers and aspect ratios are given as well as statistics forprolates and the conditional fluid. Figure 8 shows a clear dependence of particle andconditional fluid acceleration norm on particle inertia and shape in the near-wall region. Obviously, mean and RMS of both particles and conditioned fluid increase with increasing aspect ratio and decrease with increasing inertia. These trends are more pronounced for the acceleration norm RMS profiles. The profile of the mean acceleration norm of the

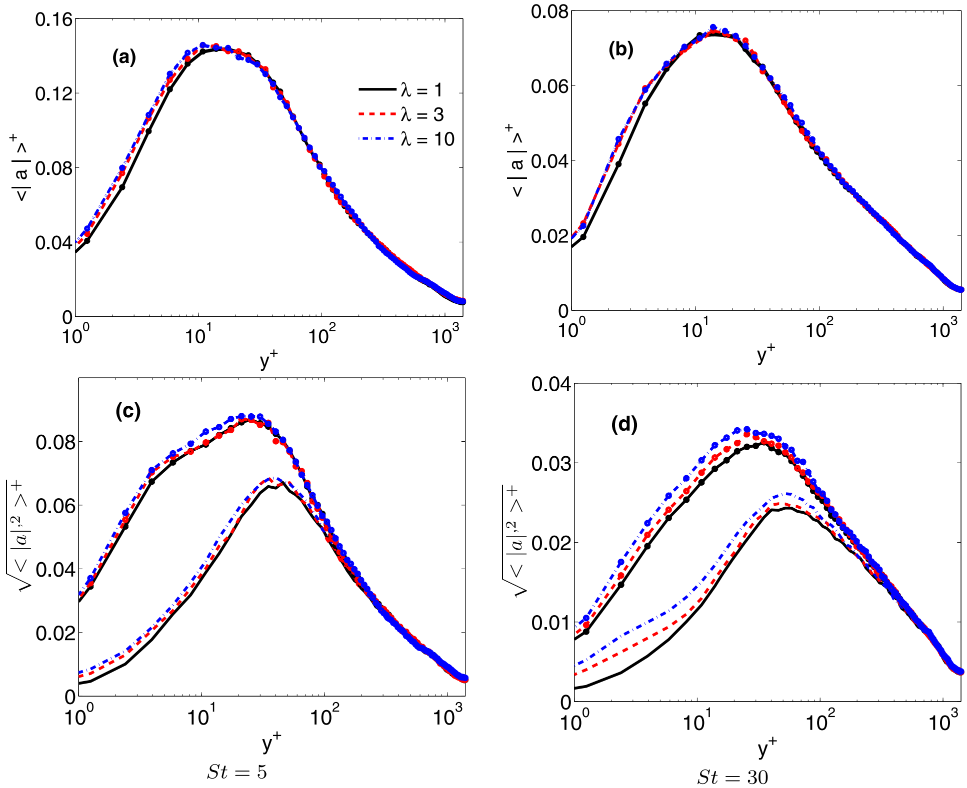

Figure 8. Mean (a,b) and RMS (c,d) of the particles and conditional fluid norm of acceleration. Particles: lines with symbols. Conditional fluid: lines. Left: $St = 5$, right: $St = 30$.

particles collapses with that of the corresponding conditioned fluid, whatever the particle inertia. On the opposite, particle acceleration RMS departs upward from that of the corresponding conditional fluid,regardless of the aspect ratio and inertia. According to the above discussion, this is intimately related to the elongation effects on selective sampling and the mean drag undergone by the particles. Indeed, mean particle acceleration can also be seen as a mean drag force per unit mass experienced by the particles along their trajectories, thus due to the different elongations and orientations, spheroids undergo different mean drag. Consequently, drifting towards the wall, spheroids with different elongations do not see, statistically, the same fluid acceleration.

6. Acceleration PDF

Besides the investigation of the inertia and shape effects on the mean and RMS of the acceleration, it is interesting to analyse these effects on the acceleration probability distribution function. PDFs of the normalised acceleration in the streamwise and wall-normal directions obtained at different wall distances are depicted in Figures 9 and 10, respectively. To emphasise the tails of the PDFs, a semi-logarithmic scale is used.

Figure 9 shows that PDFs of the normalised streamwise acceleration exhibit a dominance of large positive acceleration away from the wall. In opposite, near the wall,

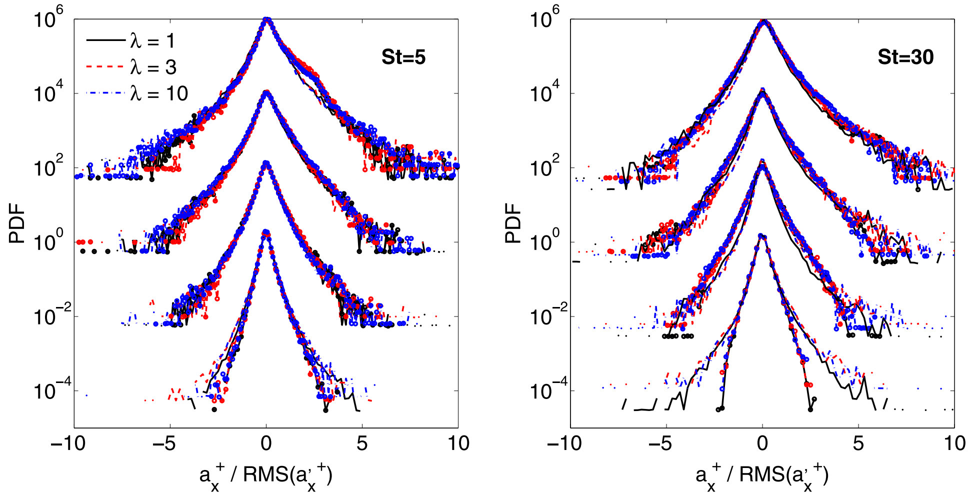

Figure 9. Normalised PDFs of streamwise acceleration. For each plot from top to bottom: $y^+ = 1000$, $y^+ = 500$, $y^+ = 200$ and $y^+ = 20$. All plots are shifted up by 100 units. Particles: lines with symbols. Conditional fluid: lines.

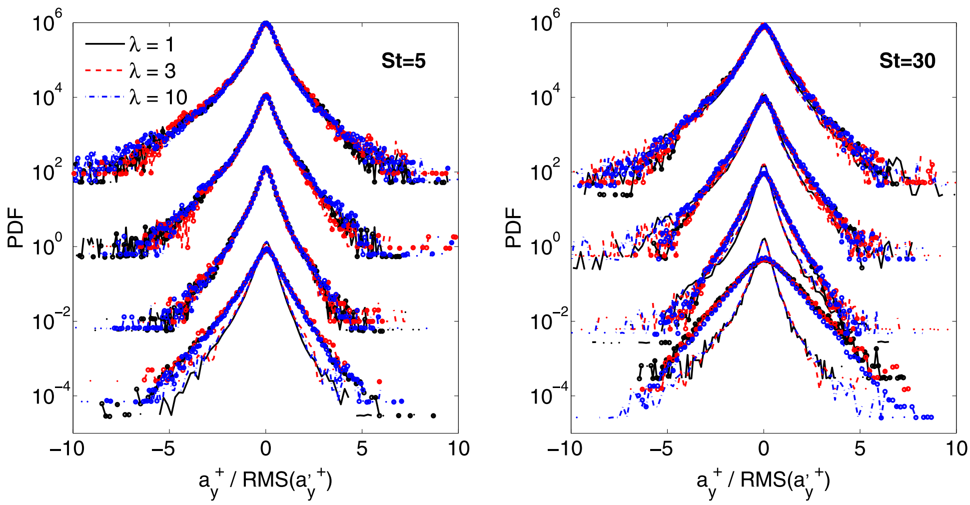

Figure 10. Normalised PDFs of wall-normal acceleration. For each plot from top to bottom: $y^+ = 1000$, $y^+ = 500$, $y^+ = 200$ and $y^+ = 20$. All plots are shifted up by 100 units. Particles: lines with symbols. Conditional fluid: lines.

deceleration is more dominant since the peak of PDFs shifts to smaller negative values. This is consistent with the profile of the mean streamwise acceleration, depictedin Figure 4. As found in earlier studies [19,21], the PDFs of particle streamwise acceleration depart from that of the fluid seen and their tails become narrower as the wall is approached. This behaviour is also observed when the Stokes number is increased, regardless of the aspect ratio. This has already been observed for spherical particles [21] and attributed to the filtering effect of inertia. Moreover, whatever the aspect ratio and inertia, PDFs of the particles streamwise acceleration remain similar to that of spherical particles, except at the PDF tails, where a slight dependence on particle elongation is noticed. This is also the case for the conditional fluid, implying that the shape effect observed for the mean and RMS of the streamwise component arise mainly at large streamwise acceleration.

As mentioned in the introduction, the particle acceleration wall-normal component has been investigated in previous studies, by Zamansky et al. [21] in the case of spheres and by Njobuwenwu and Fairweather [22] for spheroids. Zamansky et al. [21] only reported results away from the wall, at $y^+ = 100$. They showed a slight effect of inertia, leading to narrower PDF tails compared to the conditional fluid. Njobuwenwu and Fairweather [22] did not observe a significant effect of the wall distance nor of particle shape on the tails of particle acceleration PDFs. As depicted in Figure 10, in opposite to the streamwise component, PDFs of thenormalised wall-normal acceleration show that, consistently tothe mean acceleration profiles, deceleration is more likely experienced by theparticles in the core of the channel, whereas a positive wall-normal accelerationdominates near the wall. In addition, as the wall is approached, wall-normal particleaccelerations exhibit fat-tailed PDFs. This trend is more pronounced for the higherinertia $St = 30$ case. This means that particles present a higher probability forexperiencing higher wall-normal acceleration compared to the conditional fluid. Thecounterbalance effect is seen at the peak of PDFs since the conditional fluid exhibits ahigher probability of low wall-normal acceleration compared to the particles.Clearly, the effect of the wall and inertia is a deviation from conditional fluidto fat-tailed PDFs of the particles wall-normal acceleration. Moreover, theeffect of particle elongations is similar to that observed for the streamwisecomponent. Namely, a similar trend compared to spherical particles and a weakeffect on the PDF tails for both particles and conditional fluid are observed.

7. Acceleration autocorrelation

For further insight into the behaviour of prolate spheroid acceleration, we depict the streamwise and wall-normal Lagrangian autocorrelation coefficients obtained for different wall distances in Figure 11. This autocorrelation is computed along the trajectories of a set of particles located at a distance y_0 from the wall at the time t_0 according to

$$\rho_{i,j}(y_0, t) = \frac{\langle a'_i(t_0) a'_i(t_0 + t)\rangle_{y_0}}{\sqrt{\langle a'_i(t_0)^2\rangle_{y_0} \langle a'_i(t_0 + t)^2\rangle_{y_0}}} \tag{16}$$

where $a'_i(t_0 + t) = a_i(t_0 + t) - \langle a_i(t_0 + t)\rangle$ is an acceleration fluctuation. Here, brackets '$\langle . \rangle$' denote an averaging procedure over the set of prolate spheroids that were located at y_0 at t_0.

Figure 11 shows the streamwise and wall-normal acceleration autocorrelations for spherical and elongated particles as well as for the surrounding fluid at different wall distances. Due to inertia, both streamwise and wall-normal particle acceleration components are correlated over several timescales in wall units, at all wall distances. The influence of the wall is clearly noticeable, since particle acceleration autocorrelation decreases faster as the wall is approached, for all cases. These effects of wall and inertia are not significantly altered by elongation for the particle acceleration autocorrelation.

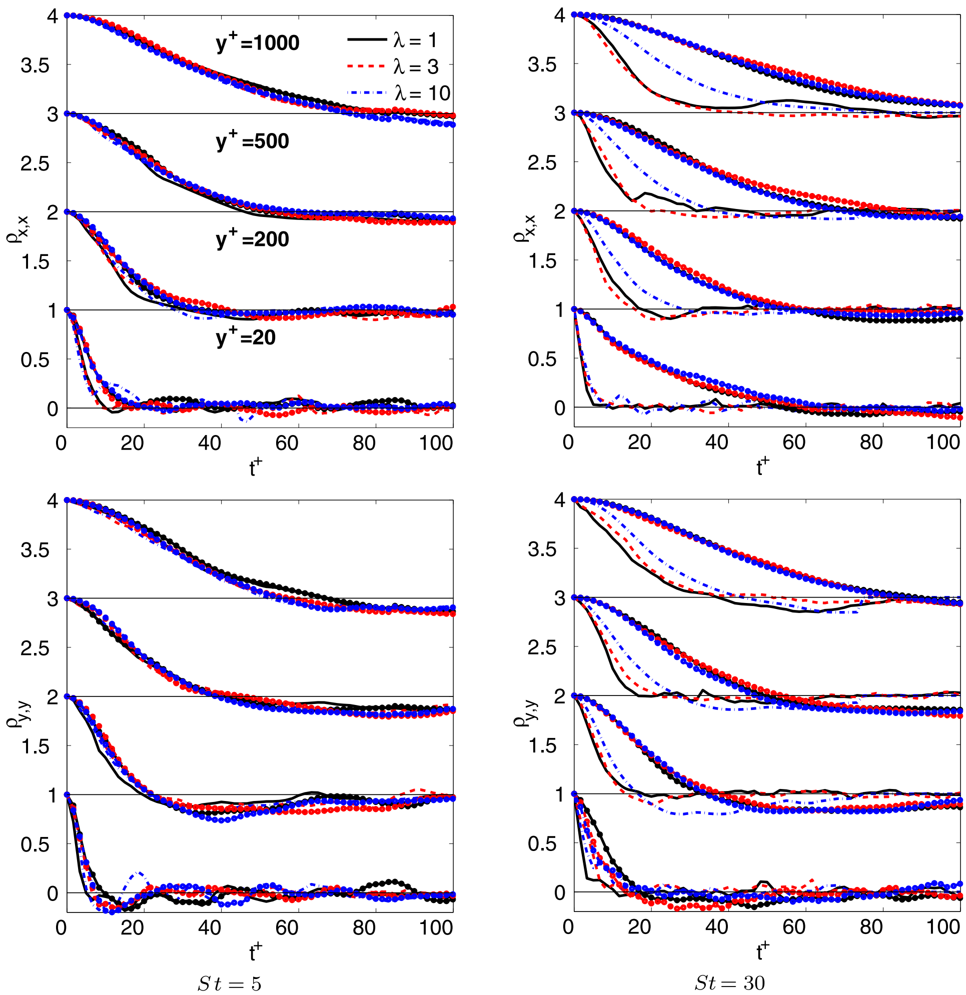

Figure 11. Particle and conditional fluid acceleration autocorrelations as a function of time. All plots are shifted up by 1 unit. Particles: lines with symbols. Conditional fluid: lines.

At higher inertia $St = 30$, particle acceleration autocorrelation departs from that of the conditional fluid, displaying a much longer decorrelation time. As mentioned above this is due to the larger response time of high inertia particles and it is consistent with earlier findings on spherical particles given by Zamansky et al. [21]. Moreover, for $St = 30$, substantial differences on the conditional fluid streamwise and wall-normal acceleration are observed for different aspect ratios. Higher aspect ratios ($\lambda = 10$) lead to longer conditional fluid acceleration autocorrelations. Both trends amplify as y^+ increases. This confirms that elongated particles with high Stokes number statistically sample regions of different fluid acceleration. At the channel centre, elongated particles with high inertia sample fluid regions with highly correlated streamwise and wall-normal accelerations.

The time at which the acceleration autocorrelation crosses zero can be extracted from Figure 11. The evolution with wall distance as well as with elongation and shape of this zero-crossing time is analysed here. This further quantifies the discussion on the acceleration

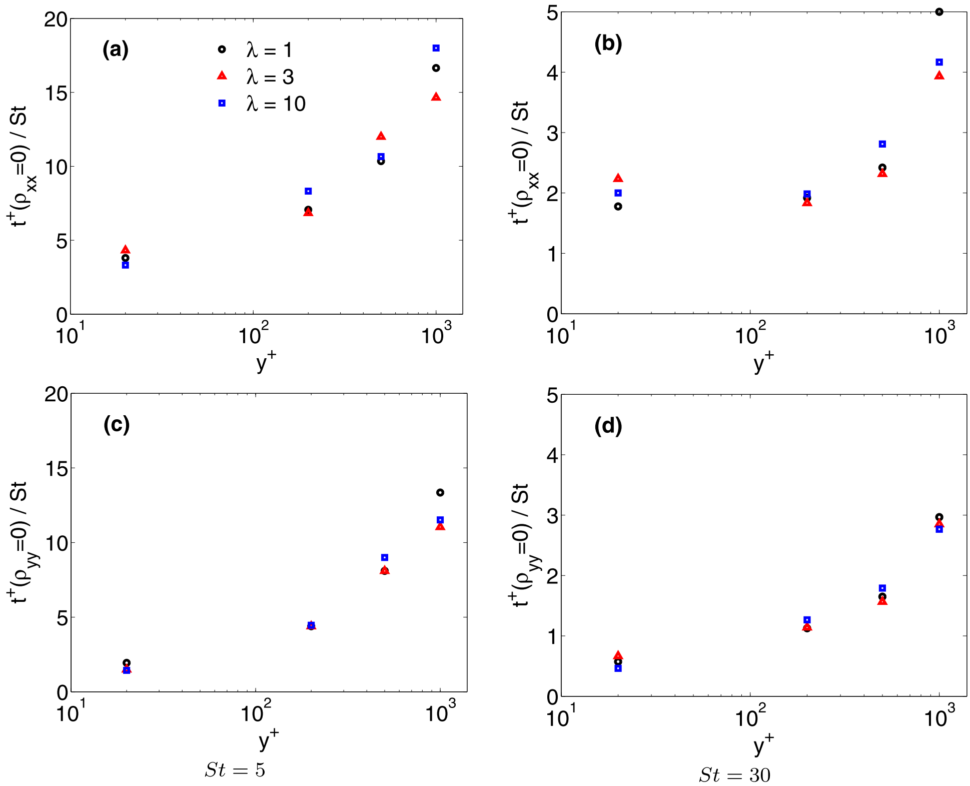

Figure 12. Normalised zero-crossing time scale as a function of wall distance.

autocorrelations given by Figure 11. In Figure 12, the zero-crossing time normalised by the Stokes number $t^+(\rho_{i,j} = 0)/St$ is plotted as a function of the wall distance for varying Stokes numbers and particle elongations. According to the discussion on the acceleration autocorrelation, $t^+(\rho_{i,j} = 0)/St$ increases as particles move away from the wall for both acceleration components. This behaviour suggests the existence of a local characteristic time scale, different from the imposed global Stokes number. This observation confirms earlier findings by Kuerten [36] and Marchioli [37] regarding the need of adjusting the particle response time to the local instantaneous flow.

Regarding the zero-crossing time obtained from the streamwise acceleration component (Figure 12(a,b)) there is a non-monotonic evolution with y^+ as a function of the aspect ratio. Elongation influences this characteristic timescale in the streamwise direction. For the wall-normal component (Figure 12(c,d)), the zero-crossing time is less influenced by changes in the aspect ratio. Moreover, for the wall-normal component, practically no differences with spheres are observed.

Zero-crossing timescales obtained for different acceleration components present roughly similar values. However, between $St = 5$ and 30, there is a factor that roughly varies between 3 and 5, confirming observations from Figure 11 on the influence of inertia on particle acceleration autocorrelations. Through the example of the zero-crossing timescale given here, it is argued that particle acceleration characteristic timescales evolve with wall distance. Moreover, this evolution is influenced by the aspect ratio in the case of elongated particles. Classifying particle behaviour in turbulent channel flow according to a global Stokes number has already been proven as inappropriate for spherical particles [36,37]. When elongation is introduced, the global Stokes number classifications can be questioned even further. The results presented here point out the need for a local dimensionless number estimation adapted to the case of prolate spheroids.

8. Conclusion

This study deals with the acceleration of spheroidal particles in a turbulent channel flow through an Eulerian–Lagrangian approach. The turbulent flow field, for $Re_\tau = 1440$, is computed by DNS, and spheroidal point particles are tracked using a Lagrangian formulation under the one-way coupling assumption. Acceleration statistics are collected for six different cases ($St = 5$ and 30 and $\lambda = 1$, 3 and 10) in a time window in which the acceleration as well as translational and rotational velocity statistics are steady. The analysis focuses on the influence of spheroid elongation and inertia on the particle acceleration statistics. In addition to this, the study deals with fluid acceleration statistics conditioned on the presence of prolate spheroids in order to describe fluid regions where particles segregate.

The results presented here show that, in agreement with earlier findings [21], particle acceleration RMS decreases with increasing inertia. In addition, for $St = 5$ the peak of the streamwise particle acceleration RMS is higher than the acceleration RMS of the conditional fluid. Furthermore, streamwise mean and RMS acceleration are, quantitatively, affected by particle elongation as the wall is approached, whereas, only a slight effect is observed on the wall-normal particle acceleration RMS. The results also point out that the norm of the particle and conditional fluid accelerations are clearly influenced by particle inertia and shape, in the near-wall region. From a physical point of view, elongation and inertia have a significant effect on the mean drag and on particle selective sampling.

Furthermore, as a consequence of the filtering effect of inertia, the normalised streamwise acceleration PDFs depart from that of the fluid seen and their tails become narrower as inertia is increased, consistent with [20,21]. This effect is more pronounced as the wall is approached, regardless of the aspect ratio. Contrarily, the wall-normal acceleration component exhibits a fat-tailed acceleration PDF. Whatever the direction, the effect of particle elongation is not clearly discernible, except on the tails of PDFs for both particle and conditional fluid acceleration PDFs.

Particle acceleration autocorrelation results remain unchanged under the influence of elongation at all wall distances. However, surrounding fluid acceleration autocorrelations show that elongated particles with high Stokes number statistically sample regions with highly correlated streamwise and wall-normal accelerations in the channel centre. The zero-crossing acceleration autocorrelation timescale is also given in this study. It evolves with wall distance as expected from the autocorrelations, and this evolution is influenced by the aspect ratio in the case of elongated particles.

The classification of elongated particle behaviour in turbulent channel flow based on a global Stokes number is questioned here. The results presented point out the need for a local dimensionless number estimation adapted to the case of spheroids. Even though globally acceleration statistics of slightly elongated inertial particles present rather small differences with spherical particles across the channel, these differences are emphasised near the wall and for increasing Stokes numbers. The complex interplay between the local evolution of the Stokes number, particle elongation and orientation as well as the influence of the wall may lead to surprising effects on acceleration statistics. For further analysing the above-mentioned trends, more aspect ratios and Stokes numbers should be explored in future studies. Coupling the Eulerian code with an immersed boundary method in order to treat finite-size elongated particles in turbulent channel flow may also lead to further insight on the problem of elongated particle interaction with wall turbulence through acceleration statistics.

In this study, gravity has been neglected in order to analyse the influence of inertia and shape on acceleration statistics and compare the findings with previous studies on spherical particle acceleration in channel flow in the absence of gravity. According to Arcen et al. [15], gravity leads to an enhancement of the relative particle/fluid velocity. Thus, the Stokes assumption on the drag force is no longer valid. Arcen et al. [15] have also shown that gravity alters particle translational and rotational statistics as well as particle distribution across the channel. Hence, there is ongoing work which includes gravity to the simulations.

Acknowledgements

M. Buffat is acknowledged for the development of the computational code. Numerical simulations were performed on the P2CHPD parallel cluster; the authors are grateful to C. Pera for the administration of this system.

Disclosure statement

No potential conflict of interest was reported by the authors.

Funding

This study received funding by the French National Research Agency (ANR)under the grant ANR-15-CE02-0013 (project WIND-OV); their support is gratefully acknowledged.

ORCID

Juan Ignacio Polanco http://orcid.org/0000-0001-7705-753X

References

[1] Mourelle D, Prieto AR. Pollen and spores from surface samples in the campos region of Uruguay and their paleoecological implications. Acta Bot Bras. 2016;30: 351–370.
[2] Koch DL, Subramanian G. Collective hydrodynamics of swimming microorganisms: living fluids. Annu Rev Fluid Mech. 2011;43:637–659.
[3] Lundell F, Söderberg LD, Alfredsson PH. Fluid mechanics of papermaking. Annu Rev Fluid Mech. 2011;43:195–217.
[4] Voth GA, Soldati A. Anisotropic particles in turbulence. Annu Rev Fluid Mech. 2017;49: 249–276.
[5] Zhang H, Ahmadi G, Fan FG, et al. Ellipsoidal particles transport and deposition in turbulent channel flows. Int J Multiph Flow. 2001;27:971–1009.
[6] Mortensen PH, Andersson H, Gillissen JJJ, et al. Dynamics of prolate ellipsoidal particles in a turbulent channel flow. Phys Fluids. 2008;20:093302.
[7] Mortensen PH, Andersson HI, Gillissen JJJ, et al. On the orientation of ellipsoidal particles in a turbulent shear flow. Int J Multiph Flow. 2008;34:678–683.
[8] Marchioli C, Fantoni M, Soldati A. Orientation, distribution, and deposition of elongated, inertial fibers in turbulent channel flow. Phys Fluids. 2010;22:033301.

[9] Zhao F, Van Wachem BGM. Direct numerical simulation of ellipsoidal particles in turbulent channel flow. Acta Mech. 2013;224:2331–2358.
[10] Zhao L, Challabotla NR, Andersson HI, et al. Rotation of nonspherical particles in turbulent channel flow. Phys Rev Lett. 2015;115:244501.
[11] Zhao L, Marchioli C, Andersson HI. Slip velocity of rigid fibers in turbulent channel flow. Phys Fluids. 2014;26:063302.
[12] Jeffery GB. The motion of ellipsoidal particles immersed in a viscous fluid. Proc R Soc Lond A. 1922;102:161–179.
[13] Happel J, Brenner H. Low Reynolds number hydrodynamics. Prentice-Hall: Springer Science & Business Media; 1965.
[14] Ouchene R, Hamidouche S, Arcen B, et al. Turbulent dispersion of ellipsoidal particles in a wall-bounded turbulent flow. 9th International Conference on Multiphase Flow; 2016.
[15] Arcen B, Ouchene R, Khalij M, et al. Prolate spheroidal particles' behavior in a vertical wall-bounded turbulent flow. Phys Fluids. 2017;29:093301.
[16] Eaton JK, Fessler JR. Preferential concentration of particles by turbulence. Int J Multiph Flow. 1994;20:169–209.
[17] Bec J, Biferale L, Boffetta G, et al. Acceleration statistics of heavy particles in turbulence. J Fluid Mech. 2006;550:349–358.
[18] Ayyalasomayajula S, Warhaft Z, Collins LR. Modeling inertial particle acceleration statistics in isotropic turbulence. Phys Fluids. 2008;20:095104.
[19] Gerashchenko S, Sharp NS, Neuscamman S, et al. Lagrangian measurements of inertial particle accelerations in a turbulent boundary layer. J Fluid Mech. 2008;617:255–281.
[20] Lavezzo V, Soldati A, Gerashchenko S, et al. On the role of gravity and shear on inertial particle accelerations in near wall turbulence. J Fluid Mech. 2010;658:229–246.
[21] Zamansky R, Vinkovic I, Gorokhovski M. Acceleration statistics of solid particles in turbulent channel flow. Phys Fluids. 2011;23:113304.
[22] Njobuenwu DO, Fairweather M. Effect of shape on inertial particle dynamics in a channel flow. Flow Turbul Combust. 2014;92:83–101.
[23] Buffat M, Le Penven L, Cadiou A. An efficient spectral method based on an orthogonal decomposition of the velocity for transition analysis in wall bounded flow. Comput Fluids. 2011;42:62–72.
[24] Maxey MR, Riley JJ. Equation of motion for a small rigid sphere in a nonuniform flow. Phys Fluids. 1983;26:883–889.
[25] Yin C, Rosendahl L, Kær SK, et al. Modelling the motion of cylindrical particles in a nonuniform flow. Chem Eng Sci. 2003;58:3489–3498.
[26] Gallily I, Cohen AH. On the orderly nature of the motion of nonspherical aerosol particles. II. Inertial collision between a spherical large droplet and an axially symmetrical elongated particle. J Colloid Interface Sci. 1979;68:338–356.
[27] Shapiro M, Goldenberg M. Deposition of glass fiber particles from turbulent air flow in a pipe. J Aerosol Sci. 1993;24:65–87.
[28] Fan FG, Ahmadi G. Dispersion of ellipsoidal particles in an isotropic pseudo-turbulent flow field. J Fluids Eng. 1995;117:154–161.
[29] Stelzenmuller N, Polanco JI, Vignal L, et al. Lagrangian acceleration statistics in a turbulent channel flow. Phys Rev Fluids. 2017;2:054602.
[30] van Wachem B, Zastawny M, Zhao F, et al. Modelling of gas–solid turbulent channel flow with non-spherical particles with large Stokes numbers. Int J Multiph Flow. 2015;68:80–92.
[31] Marchioli C, Soldati A. Mechanisms for particle transfer and segregation in a turbulent boundary layer. J Fluid Mech. 2002;468:283–315.
[32] Picciotto M, Marchioli C, Reeks MW, et al. Statistics of velocity and preferential accumulation of micro-particles in boundary layer turbulence. Nucl Eng Des. 2005;235:1239–1249.
[33] Wallace JM, Eckelmann H, Brodkey RS. The wall region in turbulent shear flow. J Fluid Mech. 1972;54:39–48.
[34] Vinkovic I, Doppler D, Lelouvetel J, et al. Direct numerical simulation of particle interaction with ejections in turbulent channel flows. Int J Multiph Flow. 2011;37:187–197.

[35] Zhao LH, Marchioli C, Andersson HI. Stokes number effects on particle slip velocity in wall-bounded turbulence and implications for dispersion models. Phys Fluids. 2012;24:021705.
[36] Kuerten JGM. Point-Particle DNS and LES of Particle-Laden Turbulent flow-a state-of-the-art review. Flow Turbul Combust. 2016;97:689–713.
[37] Marchioli C. Physics and modelling of particle deposition and resuspension in wall-bounded turbulence. In: Minier J.-P., Pozorski J., editors. Particles in wall-bounded turbulent flows: deposition, re-suspension and agglomeration. Cham: Springer; 2017. p. 151–208.